

# Transporting Task Vectors across Different Architectures without Training

Filippo Rinaldi<sup>1</sup> Aniello Panariello<sup>1</sup> Giacomo Salici<sup>1</sup> Angelo Porrello<sup>1</sup> Simone Calderara<sup>1</sup>

## Abstract

Adapting large pre-trained models to downstream tasks often produces task-specific parameter updates that are expensive to relearn for every model variant. While recent work has shown that such updates can be transferred between models with identical architectures, transferring them across models of different widths remains largely unexplored. In this work, we introduce **THESEUS**, a training-free method for transporting task-specific updates across heterogeneous models. Rather than matching parameters directly, we characterize a task update by the functional effect it induces on intermediate representations. We formalize task-vector transport as a functional matching problem on observed activations and show that, after aligning representation spaces via orthogonal Procrustes analysis, it admits a stable closed-form solution that preserves the geometry of the update. We evaluate **THESEUS** on vision and language models across different widths, showing consistent improvements over strong baselines without additional training or backpropagation. Our results show that task updates can be meaningfully transferred across architectures when task identity is defined functionally rather than parametrically.

## 1. Introduction

Large pre-trained models have become a cornerstone of modern machine learning, demonstrating remarkable performance across a wide range of tasks in computer vision (Dosovitskiy et al., 2021; He et al., 2022) and natural language processing (Brown et al., 2020; Chowdhery et al., 2023). A key factor contributing to their success is the ability to adapt these pre-trained models to downstream tasks through fine-tuning or other lightweight techniques (Houlsby et al., 2019; Liu et al., 2022). At the same time, practitioners often maintain families of models that share

<sup>1</sup>AIImageLab, University of Modena and Reggio Emilia, Modena, Italy. Correspondence to: Filippo Rinaldi <filippo.rinaldi@unimore.it>.

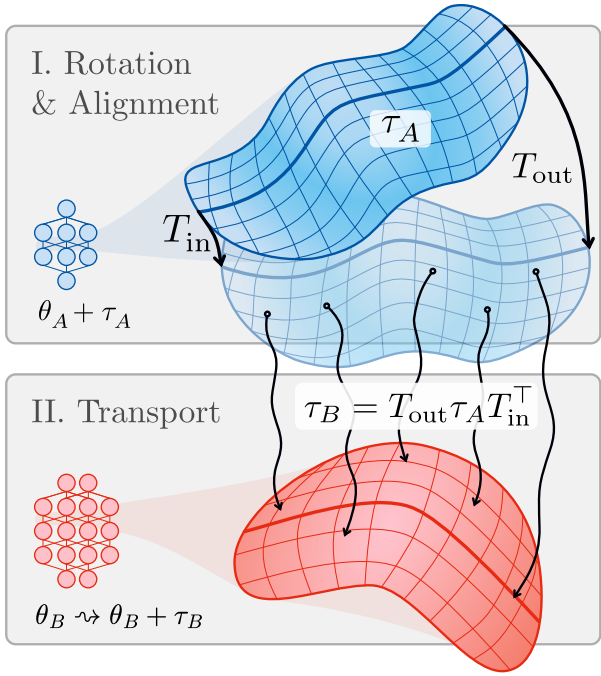


**Figure 1. Task-vector transport via orthogonal alignment.** Procrustes rotations identify shared structure between representation spaces, enabling training-free transfer of task updates across models with mismatched dimensions.

architectural similarities but differ in size, training data, or other characteristics, raising a natural question: *can a task-specific update learned by one model be transferred directly to a different one without retraining?*

Existing work on model transfer and rebasin has primarily focused on transferring knowledge between models of the same architecture and number of parameters (Ainsworth et al., 2023; Rinaldi et al., 2025). When models differ in size, however, the challenge becomes more pronounced due to the mismatch in parameter dimensions and representations. Previous approaches to this problem have relied on techniques such as knowledge distillation (Hinton et al., 2015) or fine-tuning smaller models initialized from larger ones (Turc et al., 2019; Chen et al., 2022) or vice versa (Chen et al., 2015). However, these methods usually require additional training and do not directly transfer the task-specific update itself.

In this work, we introduce a novel *task-vector transport* framework, a training-free method for transferring task-specific parameter updates between models of different sizes (Fig. 1). Rather than operating in parameter space, our approach focuses on how task updates modify intermediate representations, enabling transfer across models with mismatched widths. Our formulation is symmetric and naturally applies both to heterogeneous and identical architectures.

Despite the apparent simplicity of transferring an update between two layers, this problem is fundamentally ill-posed when models differ in width. A task update learned in one model acts on a representation space whose geometry, dimensionality, and basis are generally incompatible with those of another model. Thus, directly resizing or projecting parameters does not preserve the functional effect of the update on the model’s activations. Any meaningful transfer must therefore account for how task-specific updates interact with the internal representations induced by each model.

We address this challenge by formulating task-vector transport as a functional matching problem on observed activations. We characterize a task update by the bilinear form it induces between input and output activations of a layer, and seek a corresponding update in the target model that reproduces this effect. Since this problem is underdetermined across mismatched representation spaces, we resolve the ambiguity by aligning the representation spaces of the two models using orthogonal Procrustes analysis, which identifies shared subspaces while preserving norms and angles, yielding a closed-form, training-free transport rule.

At a conceptual level, this perspective resembles the classical Ship of Theseus (Hobbes, 1656). As model architectures evolve in width, depth, or pretraining data, their parameters may share no direct correspondence, yet we ask whether a task-specific update can still be considered the same when transferred across models. We argue that task identity should be defined by functional behavior rather than by parameter values. THESEUS embodies this view by transporting task updates in a way that preserves their effect on representations, even as the underlying model structure changes. In summary, our contributions are threefold:

- We formulate task-vector transport across heterogeneous models as a functional matching problem based on the effect of task updates on layer activations.
- We introduce a Procrustes-based alignment that embodies the transport problem with a principled geometric structure and closed-form transport rule.
- We show that THESEUS enables effective transfer of task-specific updates across models with different widths and pretraining, outperforming vision and language baselines.

## 2. Related Works

**Task updates and parameter-space transfer.** Several recent works have explored treating task-specific fine-tuning updates as first-class objects that can be manipulated, transferred, or composed in parameter space (Ilharco et al., 2023; Marczak et al., 2025; Gargiulo et al., 2025; Yadav et al., 2023). Rebasin methods exploit symmetries in neural networks to align weights across independently trained models with identical architectures, enabling interpolation or update transfer (Ainsworth et al., 2023; Singh & Jaggi, 2020; Rinaldi et al., 2025). Related lines of work study task arithmetic and model editing, where parameter differences encode task information that can be combined or reused across checkpoints (Ilharco et al., 2023; Rinaldi et al., 2026; Wortsman et al., 2022a). Recent advancements have introduced more sophisticated alignment strategies; for instance, (Nasery et al., 2025) utilize permutations and least squares to optimize neuron alignment, while (Stoica et al., 2024) enable the merging of models from distinct tasks by “zipping” similar features across layers. For transformer-based architectures, (Imfeld et al., 2024) leverage Optimal Transport to reconcile the permutation symmetries inherent in attention blocks. However, these approaches fundamentally rely on architectural equivalence and matching parameter dimensionality. When models differ in width or internal representation size, direct parameter alignment, padding, or projection no longer preserves the functional effect of the update, making the transfer problem ill-posed. Our work departs from parameter-centric alignment and instead defines task identity through its induced functional effect on representations, enabling transfer across models with mismatched widths.

### Training-based transfer and representation alignment.

A large body of work addresses transfer across heterogeneous models using training-based techniques such as knowledge distillation, teacher-student learning, or architecture-aware transformations (Hinton et al., 2015; Turc et al., 2019; Chen et al., 2015; Kangaslahti et al., 2026). While effective, these methods require additional optimization and relearn the task in the target model rather than transporting an existing update. Separately, representation alignment methods such as canonical correlation analysis and orthogonal Procrustes have been widely used to compare neural representations across models, layers, or training runs (Panariello et al., 2025; Raghu et al., 2017; Gargiulo et al., 2025; Williams et al., 2021). These techniques are typically employed as analytical tools and are not used to derive parameter updates. In contrast, we use orthogonal Procrustes alignment as a constructive mechanism to condition a functional task-matching objective, yielding a closed-form, training-free rule for transporting task updates across models with mismatched representation dimensionalities.

### 3. Method

**Setting.** Let  $\theta_A$  and  $\theta_B$  denote the parameters of the base models  $A$  and  $B$  which share the same architecture but differ in width and parameters in a given layer. We will consider  $A$  as the source model and  $B$  as the target one. Let  $\ell$  denote a linear or attention submodule (e.g., an MLP projection or an attention head projection). After fine-tuning model  $A$  on a downstream task, we define the updated weights of layer  $\ell$  as  $\theta_A^\ell + \tau_A^\ell \in \mathbb{R}^{d_{\text{out},A} \times d_{\text{in},A}}$ . Our goal is to construct a corresponding update  $\tau_B^\ell \in \mathbb{R}^{d_{\text{out},B} \times d_{\text{in},B}}$  for model  $B$  such that the function implemented by layer  $\ell$  in model  $B$  after applying the update  $\theta_B^\ell + \tau_B^\ell$  approximates the function implemented by the updated layer in model  $A$ .

Given a set of  $N$  inputs we denote the input and output activation of layer  $\ell$  in models  $A$  and  $B$  as:

$$\begin{aligned} H_{\text{in},A}^{(\ell)} &\in \mathbb{R}^{N \times L^A \times d_{\text{in},A}}, & H_{\text{out},A}^{(\ell)} &\in \mathbb{R}^{N \times L^A \times d_{\text{out},A}}, \\ H_{\text{in},B}^{(\ell)} &\in \mathbb{R}^{N \times L^B \times d_{\text{in},B}}, & H_{\text{out},B}^{(\ell)} &\in \mathbb{R}^{N \times L^B \times d_{\text{out},B}}, \end{aligned} \quad (1)$$

where  $L^A$  and  $L^B$  are the sequence lengths of models  $A$  and  $B$ , and  $d_{\text{in},A}, d_{\text{out},A}, d_{\text{in},B}, d_{\text{out},B}$  are the input and output dimensions of the layer  $\ell$  in models  $A$  and  $B$  respectively. In the following, we drop the superscript  $\ell$  to ease the notation.

**Tokens Pre-Processing.** To align the input activations of the two models, we first need to ensure that they have the same sequence length. If  $L^A < L^B$ , we interpolate the sequence length  $L^A$  to match  $L^B$  using bilinear interpolation. Then, we flatten the first two dimensions of the input activations; let  $M = N \times L^B$  be the total number of tokens after interpolation. The input activations can then be represented as:  $H_{\text{in},A} \in \mathbb{R}^{M \times d_{\text{in},A}}$  and  $H_{\text{in},B} \in \mathbb{R}^{M \times d_{\text{in},B}}$ , and similarly for the output activations. We evaluate different sequence alignment strategies in Sec. E.1.

**Objective.** We recast task-vector transport as the problem of preserving the *functional effect* of a task update on observed activations. Consider a linear layer whose output activations are given by  $H_{\text{out}} = H_{\text{in}}\theta^\top$ , where  $\theta$  are the layer weights of the base model. Applying a task update  $\tau_A$  to model  $A$  induces a change in the output activations

$$\Delta H_{\text{out},A} = H_{\text{in},A}\tau_A^\top. \quad (2)$$

This expression characterizes how the update modifies the layer outputs for the given inputs. Rather than matching  $\Delta H_{\text{out},A}$  pointwise, we characterize the update by how it *couples* input and output activations across the dataset. Specifically, we define the matrix

$$G_A = H_{\text{in},A}\tau_A^\top H_{\text{out},A}^\top \in \mathbb{R}^{M \times M}, \quad (3)$$

which aggregates the interaction between input activations, the task update, and the pre-update output representations.

#### Algorithm 1 Training-free Task-Vector Transport

---

**Require:** Source weights  $\theta_A, \theta_A^{ft}$ , target weights  $\theta_B$ , calibration dataset  $\mathcal{D}$ , scaling  $\alpha$ , sequence lengths  $L^A, L^B$ .

- 1: **for** each layer  $l \in \{1, \dots, L\}$  **do**
- 2:   Compute source task vector:  $\tau_A^l \leftarrow \theta_A^{ft,l} - \theta_A^l$
- 3:   Collect  $\{H_{in,h}, H_{out,h}\}_{h \in \{A,B\}}$  from  $\mathcal{D}$
- 4:   **if**  $L^A \neq L^B$  **then** interpolate  $\min\{L^A, L^B\}$
- 5:   Compute cross-covariances:  
 $C_{in} \leftarrow H_{in,A}^\top H_{in,B}, \quad C_{out} \leftarrow H_{out,A}^\top H_{out,B}$
- 6:   Compute SVD:  $C_{in} = U_{in}\Sigma_{in}V_{in}^\top, \quad C_{out} = U_{out}\Sigma_{out}V_{out}^\top$   $\triangleright$  Eq. (6)
- 7:   Solve orthogonal Procrustes problems:  $\triangleright$  Eq. (7)  
 $T_{in} \leftarrow U_{in}V_{in}^\top, \quad T_{out} \leftarrow U_{out}V_{out}^\top$
- 8:   Compute transported update:  $\tau_B^l \leftarrow T_{out}\tau_A^l T_{in}^\top$   $\triangleright$  Eq. (10)
- 9: **end for**
- 10: Return  $\theta_B + \alpha\tau_B$

---

For any pair of tokens  $(i, j)$ , the entry  $(G_A)_{ij}$  measures how the update-induced change at token  $i$  aligns with the original output representation at token  $j$ . Thus,  $G_A$  defines a bilinear form over token representations that captures the global functional signature of the task update on the observed data.

Thus, we seek an update  $\tau_B$  for model  $B$  whose induced bilinear form matches that of  $\tau_A$ :

$$\min_{\tau_B} \|H_{\text{in},A}\tau_A^\top H_{\text{out},A}^\top - H_{\text{in},B}\tau_B^\top H_{\text{out},B}^\top\|_F^2. \quad (4)$$

Matching these bilinear forms ensures that  $\tau_B$  reproduces the same input-output interaction structure as  $\tau_A$ , even when the two models operate in different representation spaces. While Eq. (4) provides a principled formulation of task-vector transport, it admits many equivalent solutions when the representation spaces of the two models are mismatched or only partially observed. Rather than resolving this ambiguity through direct matrix inversion, we adopt a geometric alignment strategy that explicitly enforces desirable structural properties. In particular, our design choice prioritizes norm preservation, subspace consistency, and invariance to arbitrary basis choices, while also yielding favorable numerical conditioning as a natural byproduct. The relationship with pseudo-inverse solutions and their limitations is discussed in Sec. C.

**Geometric Alignment via Procrustes.** To resolve the intrinsic ambiguity of the transport objective and to impose a principled geometric structure on the solution, we align the representation spaces of the two models via orthonormal embeddings. Concretely, we seek linear maps that embed the representation space of the source model  $A$  into that of the target model  $B$  while preserving inner products on the

shared subspace. This choice reflects a deliberate design principle: task identity should be preserved up to rotations and reflections, without introducing arbitrary rescaling or distortion. This alignment is obtained by solving two orthogonal Procrustes problems:

$$\begin{aligned} \min_{T_{\text{in}}} \|H_{\text{in},A}T_{\text{in}} - H_{\text{in},B}\|_F^2 & \quad \text{s.t.} \quad T_{\text{in}}T_{\text{in}}^\top = I_{d_{\text{in},A}}, \\ \min_{T_{\text{out}}} \|H_{\text{out},A}T_{\text{out}} - H_{\text{out},B}\|_F^2 & \quad \text{s.t.} \quad T_{\text{out}}T_{\text{out}}^\top = I_{d_{\text{out},A}}. \end{aligned} \quad (5)$$

Here  $T_{\text{in}} \in \mathbb{R}^{d_{\text{in},A} \times d_{\text{in},B}}$  and  $T_{\text{out}} \in \mathbb{R}^{d_{\text{out},A} \times d_{\text{out},B}}$  are rectangular matrices with orthonormal rows. As such, they define *isometric embeddings* from the lower-dimensional representation spaces of model  $A$  into the higher-dimensional spaces of model  $B$ . This construction naturally accommodates mismatched widths: rather than forcing a bijective correspondence between features, the Procrustes maps identify the maximally aligned subspaces shared by the two models and embed them into the target representation space. Both admit closed-form solutions via SVD of the cross-covariances  $C_{\text{in}} = H_{\text{in},A}^\top H_{\text{in},B}$ , and  $C_{\text{out}} = H_{\text{out},A}^\top H_{\text{out},B}$ :

$$C_{\text{in}} = U_{\text{in}}\Sigma_{\text{in}}V_{\text{in}}^\top, \quad C_{\text{out}} = U_{\text{out}}\Sigma_{\text{out}}V_{\text{out}}^\top, \quad (6)$$

yielding

$$T_{\text{in}} = U_{\text{in}}V_{\text{in}}^\top, \quad T_{\text{out}} = U_{\text{out}}V_{\text{out}}^\top. \quad (7)$$

The resulting embeddings are optimal in a least-squares sense: they minimize the discrepancy between the aligned activations of model  $A$  and those of model  $B$  over the sampled data. When the two representation spaces are not exactly related by an isometry, which is the typical case in practice, this alignment is necessarily approximate. The residual mismatch captures directions in the target model that have no counterpart in the source, and is intentionally ignored by the transport rule. We then express the activations of model  $B$  in terms of those of model  $A$  through the learned embeddings:

$$H_{\text{in},B} \approx H_{\text{in},A}T_{\text{in}}, \quad H_{\text{out},B} \approx H_{\text{out},A}T_{\text{out}}. \quad (8)$$

The approximation symbol emphasizes that this relation holds only on the aligned subspaces identified by Procrustes. Crucially, this approximation is not an artifact of numerical error, but a modeling choice: we restrict attention to the shared representational structure across models and deliberately ignore target-specific degrees of freedom that cannot be inferred from the source.

Substituting Eq. (8) into Eq. (4), we obtain the following *surrogate* objective:

$$\min_{\tau_B} \left\| H_{\text{in},A}\tau_A^\top H_{\text{out},A}^\top - (H_{\text{in},A}T_{\text{in}})\tau_B^\top (H_{\text{out},A}T_{\text{out}})^\top \right\|_F^2,$$

which can be rewritten as

$$\min_{\tau_B} \|H_{\text{in},A}E H_{\text{out},A}^\top\|_F^2, \quad E := \tau_A^\top - T_{\text{in}}\tau_B^\top T_{\text{out}}^\top. \quad (9)$$

This formulation restricts the transport to the maximally aligned subspaces shared by the two models. As a result, the transport preserves angles, norms, and relative geometry of the task update, while simultaneously avoiding spurious directions introduced by mismatched or unused dimensions. Under Procrustes alignment, which preserves norms and restricts attention to shared representation subspaces, the linear map  $E \mapsto H_{\text{in},A}EH_{\text{out},A}^\top$  is injective on the aligned subspace under mild rank conditions on the sampled activations. Consequently, the minimum of Eq. (9) is attained when  $E = 0$  (see Sec. A), yielding the closed-form solution:

$$\tau_B = T_{\text{out}}\tau_A T_{\text{in}}^\top. \quad (10)$$

Thus, the transported update  $\tau_B$  is obtained by rotating the task update  $\tau_A$  through orthonormal transformations that preserve its functional geometry while adapting it to the representation space of the target model. We report the whole pipeline in Algorithm 1.

### 3.1. Properties and Scope

**THESEUS Preserves the Norm.** A key property of the transport rule in Eq. (10) is that it preserves the Frobenius norm of the task update:

$$\|\tau_B\|_F = \|T_{\text{out}}\tau_A T_{\text{in}}^\top\|_F = \|\tau_A\|_F, \quad (11)$$

since  $T_{\text{in}}$  and  $T_{\text{out}}$  have orthonormal rows. This norm preservation ensures that the magnitude of the update remains consistent across models, preventing unintended scaling effects and preserving the relative strength of the task update across architectures.

**On the Generalization of THESEUS.** While we present the method assuming model  $A$  has lower-dimensional representations than model  $B$ , the formulation is symmetric. In practice, task-vector transport can be applied in either direction by swapping the roles of the two models. Moreover, when the two models have representations of equal dimensionality, the Procrustes mappings reduce to square orthogonal transformations, and the same transport rule applies without modification. We empirically study both settings in Sec. 4.

**Extension to Different Depths.** Our formulation assumes that the two models have the same number of layers, however, it can be extended to different depths by combining THESEUS with a separate layer-matching or interpolation strategy. We provide preliminary results on this extension in Sec. 4.4, leaving a detailed exploration to future work.

**Table 1. Width Scaling (Narrow → Wide).** Task-vector transport from a ViT-B/16 model pre-trained on LAION-2B ( $A$ ) to a wider ViT-B+ model pre-trained on LAION-400M ( $B$ ). Results are reported for different number of alignment batches  $\mathcal{B}$  used to estimate the Procrustes maps.  $\Delta\text{Acc}$  denotes the accuracy improvement over the zero-shot baseline of model  $B$ . THESEUS represents  $\theta_B + \tau_B$ .

Model	$\mathcal{B}$	EUROSAT	SVHN	GTSRB	RESISC45	DTD	CARS	MNIST	SUN397	AVG ( $\Delta\text{Acc}$ )
$\theta_B$ zero-shot	–	50.92	39.23	49.63	64.53	55.48	84.53	57.06	68.67	58.76 (+0.00)
$\theta_B$ fine-tune	–	98.96	91.08	98.63	92.59	77.81	87.65	99.63	76.76	90.39 (+31.63)
$\theta_A$ fine-tune	–	98.69	97.45	98.64	95.65	82.24	91.53	99.61	79.86	92.96 (+34.20)
$\theta_B + \tau_A^{\text{padded}}$	–	48.82	38.17	48.45	65.14	54.94	84.52	58.52	69.46	58.50 (-0.26)
$\theta_B + \tau_B^{\text{random}}$	–	50.63	38.96	49.65	65.65	55.58	84.56	57.39	69.60	59.00 (+0.24)
$\theta_B + \tau_{\text{pinv}}$	1	14.29	14.54	31.66	54.73	48.94	69.61	40.49	64.79	42.38 (-16.38)
$\theta_B + \tau_{\text{pinv-Tikh}}$	1	47.83	38.24	50.23	63.55	56.12	82.29	54.68	68.49	57.68 (-1.08)
$\theta_B + \tau_A^{\text{random} \rightarrow B}$	1	51.53	39.49	49.79	65.44	55.53	84.31	57.33	69.61	59.13 (+0.37)
THESEUS	1	60.41	56.80	56.62	66.98	57.23	84.62	64.49	69.60	<b>64.59 (+5.83)</b>
$\theta_B + \tau_{\text{pinv}}$	2	44.34	41.92	48.19	64.22	56.43	77.59	20.44	68.88	52.25 (-6.51)
$\theta_B + \tau_{\text{pinv-Tikh}}$	2	53.04	46.23	50.11	64.52	57.18	81.83	55.13	68.76	59.60 (+0.84)
$\theta_B + \tau_A^{\text{random} \rightarrow B}$	2	50.96	39.41	49.75	65.60	55.48	84.41	56.62	69.51	58.97 (+0.21)
THESEUS	2	64.03	59.30	59.55	68.12	57.86	84.89	68.97	70.12	<b>66.60 (+7.84)</b>
$\theta_B + \tau_{\text{pinv}}$	5	52.25	44.82	50.12	64.24	56.92	82.51	27.72	69.85	56.80 (-1.96)
$\theta_B + \tau_{\text{pinv-Tikh}}$	5	54.51	46.16	50.34	65.53	57.93	82.12	56.97	68.76	60.29 (+1.53)
$\theta_B + \tau_A^{\text{random} \rightarrow B}$	5	50.79	39.24	49.69	65.54	55.37	84.26	56.92	69.55	58.92 (+0.16)
THESEUS	5	63.59	59.61	60.46	68.40	58.83	84.85	67.01	70.35	<b>66.64 (+7.88)</b>
THESEUS	10	65.91	61.59	61.23	68.73	59.52	84.93	74.46	70.42	<b>68.35 (+9.59)</b>
THESEUS	20	67.01	62.52	61.01	69.27	60.48	85.04	76.66	70.65	<b>69.08 (+10.32)</b>

## 4. Experiments

We evaluate the efficacy of our proposed transport method across diverse vision and language benchmarks. Our experimental evaluation is organized into three investigations. First, we assess the efficacy of our training-free functional matching approach by transporting updates between models of **different widths**. Second, we evaluate the effect of our approach on different pre-trainings by focusing on models with **identical architectures**. This setting enables direct comparison with prior rebasin methods. Finally, we go beyond the limits of our framework and evaluate it in a challenging regime, where both depth and width differ (*e.g.*, ViT-B → ViT-L), showing that THESEUS enables transport across **different widths and depths**.

### 4.1. Experimental Setting

In all experiments, task-specific updates are obtained by fine-tuning a source model on the downstream task and are transported to a target model using our method, without performing any additional optimization on the target. We consider few-shot regimes with varying amounts of data used to characterize the representation spaces, and report results on standard vision and language benchmarks following established evaluation protocols. Full details on model architectures, training hyperparameters, few-shot protocols, and evaluation settings are provided in Sec. D.

**Update Scaling.** Following standard practice in the task-vector and model editing literature (Ilharco et al., 2023; Gargiulo et al., 2025; Marczak et al., 2025; Yadav et al., 2023; Rinaldi et al., 2025; Wortsman et al., 2022b), we integrate the transported update into the base model through a scalar interpolation  $\alpha$ , chosen via a validation set, applied as  $\theta + \alpha\tau$ . All reported results correspond to the value of  $\alpha$  that achieves the best performance in a linear search.

### 4.2. Transfer across Mismatched Widths

**Vision.** We first evaluate task-vector transport across models of differing widths in a vision setting. Specifically, we transport task updates  $\tau_A$  learned by a CLIP ViT-B/16 model pre-trained on LAION-2B to a wider variant of the ViT-B/16 named ViT-B/16+ from OpenCLIP (Cherti et al., 2023), pre-trained on LAION-400M. To further validate the robustness of our framework, we also perform the transport from the wider to the smaller model ( $B \rightarrow A$ ). In this latter configuration, we substitute the original source model with a ViT-B/16 pre-trained on the high-performance DataComp-XL dataset, which serves as the new target model. This allows us to assess whether updates can be successfully integrated into a target architecture that already possesses superior zero-shot capabilities. We conduct a comprehensive evaluation on the widely-used 8-Vision benchmark (Ilharco et al., 2023), more details are reported in Sec. F.1

**Baselines.** For width upscaling transfer ( $A \rightarrow B$ ), we compare our method against several baselines in Tab. 1 spanning performance bounds, naive parameter manipulations, and alternative functional matching strategies. We report the zero-shot performance of the target model  $B$  as a lower bound, and the results of fully fine-tuning models  $A$  and  $B$  as upper bounds. As naive parameter-space baselines we include: (i) zero-padding the source update  $\tau_A$  to match the dimensionality of model  $B$ , and (ii) adding a randomly initialized update to model  $B$ . Both ignore representation alignment and highlight that dimensional compatibility alone does not preserve task-specific behavior.

We also evaluate a pseudo-inverse transport baseline ( $\tau_{\text{pinv}}$ ), which solves the objective in Eq. (4) using the Moore–Penrose pseudo-inverse of the activation Gram matrices. In practice, this baseline is enabled by the truncated SVD approximation used by `torch.linalg.pinv`, which is more stable as the number of alignment batches  $\mathcal{B}$  grows, but remains unreliable in low-sample regimes. We further consider a Tikhonov-regularized variant ( $\tau_{\text{pinv-Tikh}}$ ), which improves numerical stability by penalizing large update norms but still lacks explicit representation alignment. Finally, we report a randomized alignment baseline ( $\tau_A^{\text{random} \rightarrow B}$ ), where a random source update is transported via our Procrustes maps, isolating the effect of alignment.

**Results.** As shown in Tab. 1, our Procrustes-conditioned method consistently outperforms the zero-shot baseline for the forward transfer ( $A \rightarrow B$ ) across all  $\mathcal{B}$ -shot regimes, without requiring any additional training or gradient-based updates on the target model. While a gap to supervised fine-tuning remains, the method recovers a significant fraction of the achievable gains, with the largest relative improvements in low-shot settings; additional results for the  $\mathcal{K}$ -shot protocol and for the reverse transport ( $B \rightarrow A$ ) are reported in Sec. E, where we observe similarly improvements.

In the reverse setting, the target model  $A$  is pre-trained on DataComp–XL, which provides an higher zero-shot baseline compared to the forward experiments. Our method consistently improves performance even in this high-accuracy regime indicating that task-vector transport is not limited to enhancing weaker models, but can also inject task-specific knowledge into already strong base models. In both transfer directions, the proposed SVD-based alignment exhibits markedly superior stability compared to direct matrix-inversion strategies. In the lowest-shot regimes, the standard pseudo-inverse baseline performs poorly due to rank-deficient activation Gram matrices. Even when augmented with norm-based regularization, the pseudo-inverse approach remains less stable and consistently underperforms our closed-form transport rule, highlighting the benefits of explicitly identifying shared representation subspaces via orthogonal alignment.

Table 2. Performance of linear probing with and without the application of  $\tau_A$  with best  $\alpha$  per dataset. Results are reported for different numbers of  $\mathcal{B}$ . Source: t5-3b, Target: t5-lg. THESEUS represents  $\theta_B + \tau_B$ .

Encoder	$\mathcal{B}$	MNLI	QNLI	RTE	SCITAIL	SNLI	AVG ( $\Delta\text{Acc}$ )
$\theta_A$ fine-tune	All	89.88	95.78	87.73	92.45	90.45	91.26 (-)
$\theta_B$ fine-tune	All	86.34	92.14	81.23	91.12	88.75	87.92 (-)
$\theta_A$	20	66.84	80.85	71.84	69.40	45.06	66.80 (+8.39)
$\theta_B$	20	64.87	66.61	64.62	49.85	43.42	57.87 (+0.00)
THESEUS	20	78.67	86.09	74.00	84.74	76.04	79.91 (+22.04)
$\theta_A$	50	74.91	82.43	74.01	68.67	72.61	74.53 (-2.25)
$\theta_B$	50	78.58	81.79	76.17	75.15	72.20	76.78 (+0.00)
THESEUS	50	81.81	89.10	80.90	88.30	80.30	84.08 (+7.30)
$\theta_A$	100	80.14	90.59	79.42	82.06	80.78	82.60 (+0.69)
$\theta_B$	100	81.04	84.55	81.59	82.36	80.02	81.91 (+0.00)
THESEUS	100	83.60	90.70	83.80	89.00	82.10	85.84 (+3.93)

**Language.** To assess whether task-vector transport generalizes beyond vision models, we evaluate THESEUS in a language setting using encoder–decoder Transformer architectures (Raffel et al., 2020). We consider T5–3B as the source model  $A$  and T5–Large as the target model  $B$ . In this context, both models are treated as consisting of a text encoder ( $\theta$ ) followed by a task-specific classification head ( $\omega$ ). Our protocol is designed to isolate the effect of the transported *encoder* representations. We first fine-tune the model  $A$  on each downstream task, computing a task-specific update  $\tau_A$ , for the encoder  $\theta_A$ . We then transport this encoder update to model  $B$  using THESEUS, yielding an updated encoder  $\theta_B + \tau_A$ .

To evaluate the quality of the learned representations, we adopt a linear probing protocol (Alain & Bengio, 2017). In all experiments, encoder parameters are kept strictly frozen, and a newly initialized linear classification head is trained from scratch. We consider three fixed encoders: the source encoder  $\theta_A$ , the target encoder  $\theta_B$ , and the target encoder augmented with the transported task update,  $\theta_B + \tau_A$  (THESEUS). All heads are trained under identical optimization settings, ensuring that performance differences reflect solely the quality of the underlying representations rather than any additional encoder fine-tuning.

We evaluate this setup on five closed-vocabulary natural language inference tasks from the GLUE benchmark (Wang et al., 2018). We vary the number of batches  $\mathcal{B}$  used to estimate the Procrustes maps and to train the classifier, using the same data budget for all methods. A detailed description of datasets and preprocessing is provided in Sec. F.2. This evaluation protocol allows us to directly measure how much task-relevant structure is transferred by THESEUS into the representation space of the target encoder, without interference from further encoder fine-tuning. By constraining adaptation to a linear classifier, we test whether the transported update reorganizes the target representation space in a task-aware manner. An additional transport experiment is presented in Sec. E.3 following Rinaldi et al. (2025).

**Table 3. Identical Architecture Transfer.** Task-vector transport between ViT-B/16 models with identical architectures but different pre-training ( $A$ : DataComp-XL  $\rightarrow B$ : LAION-2B). Results are reported for varying support set sizes  $\mathcal{K}$  used for alignment or optimization.  $\Delta\text{Acc}$  denotes the average accuracy improvement over the zero-shot baseline of model  $B$ . The **No Grad.** column indicates whether the method requires gradient-based optimization. THESEUS represents  $\theta_B + \tau_B$ .

Model	$\mathcal{K}$	No Grad.	EUROSAT	SVHN	GTSRB	RESISC45	DTD	CARS	MNIST	SUN397	AVG ( $\Delta\text{Acc}$ )
$\theta_B$ zero-shot	–	✓	49.41	50.58	48.29	67.98	55.96	84.50	57.10	68.70	60.31 (+0.00)
$\theta_B$ fine-tune	–	✗	98.70	97.45	98.65	95.66	83.19	88.10	99.60	77.20	92.32 (+32.01)
$\theta_B + \tau_A^{\text{unaligned}}$	–	✓	49.58	50.84	49.31	67.87	56.27	84.60	57.40	68.90	60.60 (+0.29)
TransFusion	–	✓	50.12	67.99	50.24	53.26	56.70	84.96	59.26	69.12	61.46 (+1.15)
GradFix	1	✗	61.94	71.07	60.88	70.05	58.32	87.95	86.39	72.67	71.16 (+10.85)
THESEUS	1	✓	58.64	71.38	60.30	71.95	59.79	88.89	87.17	73.08	<b>71.40 (+11.09)</b>
GradFix	2	✗	65.07	70.19	64.33	71.42	58.51	87.15	88.38	72.92	72.25 (+11.94)
THESEUS	2	✓	65.49	75.66	62.67	72.38	60.48	88.85	91.56	73.02	<b>73.76 (+13.45)</b>
GradFix	5	✗	66.05	73.59	66.61	71.57	60.02	86.82	89.06	72.97	73.34 (+13.03)
THESEUS	5	✓	66.12	72.09	61.82	73.33	61.48	88.80	93.03	73.19	<b>73.73 (+13.42)</b>
GradFix	10	✗	66.59	74.82	66.02	72.05	60.18	86.64	89.67	73.18	73.64 (+13.33)
THESEUS	10	✓	65.21	73.95	63.46	74.09	62.29	88.83	92.48	73.21	<b>74.19 (+13.88)</b>
GradFix	20	✗	67.05	74.11	66.42	72.29	60.92	85.99	89.63	73.06	73.68 (+13.37)
THESEUS	20	✓	68.42	74.82	65.73	74.16	63.77	88.92	94.62	73.33	<b>75.47 (+15.16)</b>

As shown in Tab. 2, transporting the encoder update from T5-3B to T5-Large consistently improves linear probing performance across all evaluated tasks and data regimes. While a performance gap relative to fully fine-tuned models remains, THESEUS recovers a substantial fraction of the task-specific signal using only forward passes and closed-form alignment. Moreover, performance improves monotonically as the number of alignment batches  $\mathcal{B}$  increases, indicating that richer activation statistics enable a more accurate characterization of the linguistic representation spaces.

These results demonstrate that functional task-vector transport extends beyond vision models and applies effectively to encoder-decoder language architectures, despite their additional structural complexity, showcasing the adaptability of our approach.

### 4.3. Transfer on Identical Architectures

We further evaluate our Procrustes-conditioned transport in a controlled setting where models share an identical ViT-B/16 architecture but differ only in their pre-training distributions. Specifically, we transport task updates from a source model  $A$  pre-trained on DataComp-XL to a target model  $B$  pre-trained on LAION-2B. This configuration mirrors the evaluation protocol established by GradFix (Rinaldi et al., 2026), enabling a direct and fair comparison with existing task-vector transport methods, including TransFusion (Rinaldi et al., 2025) and GradFix. To maintain methodological consistency with these baselines, we utilize a standard  $\mathcal{K}$ -shot evaluation protocol, where  $\mathcal{K}$  denotes the number of examples per class used for representation alignment or, in the case of GradFix, gradient-based optimization.

Results are reported in Tab. 3, showing that our method consistently outperforms TransFusion across all shot regimes and remains highly competitive with GradFix under identical architectural and evaluation conditions. Notably, while GradFix relies on multiple backward passes and iterative optimization, our approach achieves comparable or superior performance using only forward passes and a closed-form rule, making it significantly more scalable. Moreover, as the number of available examples increases, our method exhibits more favorable performance gains, matching or exceeding GradFix in higher-shot regimes.

These results highlight a key advantage of our approach: task-vector transport can be performed efficiently and training-free even when models share the same architecture, without sacrificing performance. This demonstrates that functional matching via orthogonal alignment provides a robust alternative to gradient-based task-vector transfer, extending naturally from heterogeneous architectures to identical-architecture settings.

### 4.4. Transfer across Depth and Width

We finally assess the structural generalization of task-vector transport by considering transfers between models that differ in both depth and width. Specifically, we transport task updates from a ViT-B/16 source model  $A$  to a ViT-L/14 target model  $B$ , with both models pre-trained on the DataComp-XL distribution. This scenario is particularly challenging, as it requires reconciling mismatches not only in representation dimensionality but also in the number of transformer blocks.

**Table 4. Depth and Width Scaling.** Task-vector transport from a ViT-B/16 model to a ViT-L/14 model, both pre-trained on DataComp-XL. This setting involves simultaneous depth and width mismatches and employs naive layer interpolation to align transformer depth prior to transport. Results are reported for  $B = 10$  alignment batches.  $\Delta\text{Acc}$  denotes the average accuracy improvement over the zero-shot baseline of model  $B$ . THESEUS represents  $\theta_B + \tau_B$ .

Model	$B$	EUROSAT	SVHN	GTSRB	RESISC45	DTD	CARS	MNIST	SUN397	AVG ( $\Delta\text{Acc}$ )
$\theta_B$ zero-shot	–	68.40	67.44	58.96	71.27	66.81	93.01	86.84	76.34	73.63 (+0.00)
$\theta_A$ fine-tune	–	98.66	97.70	98.77	95.40	83.29	92.43	99.64	79.91	93.23 (+19.60)
$\theta_B$ fine-tune	–	99.00	98.22	98.42	96.73	86.88	94.80	99.76	82.94	94.59 (+20.96)
THESEUS	10	76.78	78.34	73.59	75.02	72.71	93.10	95.18	77.16	<b>80.24 (+6.61)</b>

To address the depth mismatch, we adopt a simple interpolation-based strategy. We uniformly expand the transformer blocks of both the base model  $A$  and its fine-tuned counterpart  $A^{ft}$  to match the depth of the ViT-L architecture by interpolating weights in layer space. This yields a depth-aligned version of model  $A$ , from which we compute an enlarged task update  $\tau_A$ . We then apply our Procrustes-conditioned transport rule to account for the remaining width difference between the two architectures. We emphasize that this depth-alignment procedure is intentionally naive and serves only to demonstrate feasibility, rather than to provide an optimal solution for depth scaling.

As shown in Tab. 4, THESEUS enables effective task-vector transport even under simultaneous changes in depth and width. Without performing any additional training or gradient-based updates on the target model, the transported updates consistently improve upon the ViT-L zero-shot baseline across benchmarks. These results indicate that the proposed functional matching framework extends beyond identical-depth architectures and remains effective under structural scaling. A more principled treatment of depth alignment is an important direction for future work.

#### 4.5. THESEUS as Warm-Start for Fine-Tuning

Finally, we investigate whether THESEUS can improve downstream fine-tuning efficiency by providing a strong initialization for subsequent optimization. Specifically, we use the transported task vector to initialize the target model  $\theta_B$  prior to standard supervised fine-tuning. Fig. 2 reports the average loss and accuracy over eight vision classification tasks during the first training steps, capturing the early convergence before all models reach similar minima. Models with THESEUS start with a better initialization, exhibiting lower initial loss and higher accuracy than the standard pre-trained baseline. This warm-start effect is particularly evident in the convergence dynamics: the 10-batch alignment variant achieves after only 50 steps what the baseline  $\theta_B$  reaches after 150 steps. Overall, these results indicate that THESEUS not only enables effective zero-shot adaptation but also serves as a practical initialization strategy that reduces the computational cost of supervised fine-tuning.

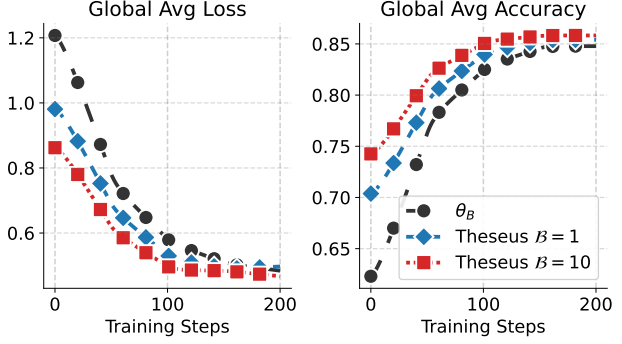


**Figure 2. Comparative Analysis of Convergence Trends.** Global average validation loss and accuracy across eight datasets. We compare standard fine-tuning from baseline  $\theta_B$  against initialization via our approach.

## 5. Conclusions

In this work, we introduced THESEUS, a training-free framework for transporting task-specific updates across pre-trained heterogeneous models. By formulating task-vector transfer as a functional matching problem and conditioning it through orthogonal Procrustes alignment, THESEUS yields a simple closed-form transport rule that preserves the geometric structure of task updates while naturally accommodating mismatches in representation dimensionality.

Across a wide range of vision and language experiments, we demonstrated that THESEUS enables effective transfer of task knowledge across models of different widths, pre-training distributions, and, as an extension, architectural depths. The method consistently outperforms naive baselines and direct pseudo-inverse approaches, while remaining competitive with gradient-based alternatives when architectures match, despite requiring only forward passes. We also showed that transported task vectors provide a strong initialization for downstream fine-tuning, accelerating convergence. Overall, our results support a functional view of task identity, in which task-specific knowledge is defined by its effect on representations rather than by a fixed parameterization. This perspective opens new directions for model reuse, modular adaptation, and efficient deployment of large pre-trained systems.

## Impact Statement

This work introduces THESEUS, a training-free approach for transferring task-specific updates across pre-trained models by matching their functional effect on internal representations. By enabling reuse of task adaptations without additional optimization, our method has the potential to reduce computational costs, energy consumption, and environmental impact associated with repeatedly fine-tuning large models. This can facilitate more efficient deployment of machine learning systems, especially in resource-constrained settings or when adapting models across evolving architectures.

The proposed framework may also support more modular and sustainable model development practices, allowing practitioners to share and reuse task knowledge across model variants without access to original training data. However, as with any method that enables model adaptation, care should be taken to ensure that transferred task updates do not propagate unintended biases or harmful behaviors learned during fine-tuning. Our method preserves functional behavior by design, and thus inherits both the strengths and limitations of the source task updates.

We do not foresee direct misuse scenarios unique to THESEUS beyond those already present in standard fine-tuning and model reuse pipelines. Nonetheless, responsible deployment should include appropriate evaluation and monitoring when transferring task updates across domains or applications. We hope this work encourages further research into efficient, transparent, and accountable mechanisms for model adaptation.

## References

Ainsworth, S. K., Hayase, J., and Srinivasa, S. S. Git re-basin: Merging models modulo permutation symmetries. In *International Conference on Learning Representations*, 2023.

Alain, G. and Bengio, Y. Understanding intermediate layers using linear classifier probes. In *International Conference on Learning Representations*, 2017.

Brown, T. B., Mann, B., Ryder, N., Subbiah, M., Kaplan, J., Dhariwal, P., Neelakantan, A., Shyam, P., Sastry, G., Askell, A., Agarwal, S., Herbert-Voss, A., Krueger, G., Henighan, T., Child, R., Ramesh, A., Ziegler, D. M., Wu, J., Winter, C., Hesse, C., Chen, M., Sigler, E., Litwin, M., Gray, S., Chess, B., Clark, J., Berner, C., McCandlish, S., Radford, A., Sutskever, I., and Amodei, D. Language models are few-shot learners. *Advances in Neural Information Processing Systems*, 2020.

Chen, B., Bakhshi, A., Batista, G., Ng, B., and Chin, T.-J. Update compression for deep neural networks on the edge. In *IEEE International Conference on Computer Vision and Pattern Recognition Workshops*, 2022.

Chen, T., Goodfellow, I., and Shlens, J. Net2net: Accelerating learning via knowledge transfer. In *International Conference on Learning Representations*, 2015.

Cheng, G., Han, J., and Lu, X. Remote Sensing Image Scene Classification: Benchmark and State of the Art. *Proceedings of the IEEE*, 2017.

Cherti, M., Beaumont, R., Wightman, R., Wortsman, M., Ilharco, G., Gordon, C., Schuhmann, C., Schmidt, L., and Jitsev, J. Reproducible scaling laws for contrastive language-image learning. In *Proceedings of the IEEE conference on Computer Vision and Pattern Recognition*, 2023.

Chowdhery, A., Narang, S., Devlin, J., Bosma, M., Mishra, G., Roberts, A., Barham, P., Chung, H. W., Sutton, C., Gehrmann, S., et al. Palm: Scaling language modeling with pathways. *Journal of Machine Learning Research*, 2023.

Cimpoi, M., Maji, S., Kokkinos, I., Mohamed, S., and Vedaldi, A. Describing textures in the wild. In *Proceedings of the IEEE conference on Computer Vision and Pattern Recognition*, 2014.

Dosovitskiy, A., Beyer, L., Kolesnikov, A., Weissenborn, D., Zhai, X., Unterthiner, T., Dehghani, M., Minderer, M., Heigold, G., Gelly, S., Uszkoreit, J., and Houlsby, N. An image is worth 16x16 words: Transformers for image recognition at scale. In *International Conference on Learning Representations*, 2021.

Gargiulo, A. A., Crisostomi, D., Bucarelli, M. S., Scardapane, S., Silvestri, F., and Rodolà, E. Task singular vectors: Reducing task interference in model merging. *Proceedings of the IEEE conference on Computer Vision and Pattern Recognition*, 2025.

Group, S. N. et al. The stanford natural language inference (snli) corpus, 2022.

He, K., Chen, X., Xie, S., Li, Y., Dollár, P., and Girshick, R. Masked autoencoders are scalable vision learners. In *Proceedings of the IEEE conference on Computer Vision and Pattern Recognition*, 2022.

Helber, P., Bischke, B., Dengel, A., and Borth, D. Eurosat: A novel dataset and deep learning benchmark for land use and land cover classification. *Journal of Selected Topics in Applied Earth Observations and Remote Sensing*, 2019.

Hinton, G., Vinyals, O., and Dean, J. Distilling the knowledge in a neural network. *Neural Information Processing Systems Workshops*, 2015.

Hobbes, T. *Elements of Philosophy, the First Section, Concerning Body*. London: R & W Leybourn., 1656.

Houlsby, N., Giurgiu, A., Jastrzebski, S., Morrone, B., De Laroussilhe, Q., Gesmundo, A., Attariyan, M., and Gelly, S. Parameter-efficient transfer learning for nlp. In *International Conference on Machine Learning*, 2019.

Ilharco, G., Ribeiro, M. T., Wortsman, M., Schmidt, L., Hajishirzi, H., and Farhadi, A. Editing models with task arithmetic. In *International Conference on Learning Representations*, 2023.

Imfeld, M., Graldi, J., Giordano, M., Hofmann, T., Anagnosidis, S., and Singh, S. P. Transformer Fusion with Optimal Transport. In *International Conference on Learning Representations*, 2024.

Kangaslahti, S., Nayak, N. V., Geuter, J., Fumero, M., Locatello, F., and Alvarez-Melis, D. Boomerang distillation enables zero-shot model size interpolation. In *International Conference on Learning Representations*, 2026.

Khot, T., Sabharwal, A., and Clark, P. Scitail: A textual entailment dataset from science question answering. In *Proceedings of the AAAI Conference on Artificial Intelligence*, volume 32, 2018.

Krause, J., Stark, M., Deng, J., and Fei-Fei, L. 3D Object representations for fine-grained categorization. In *IEEE International Conference on Computer Vision Workshops*, 2013.

Lecun, Y., Bottou, L., Bengio, Y., and Haffner, P. Gradient-based learning applied to document recognition. *Proceedings of the IEEE*, 86(11):2278–2324, 1998. doi: 10.1109/5.726791.

Liu, H., Tam, D., Muqeeth, M., Mohta, J., Huang, T., Bansal, M., and Raffel, C. A. Few-shot parameter-efficient fine-tuning is better and cheaper than in-context learning. In *Advances in Neural Information Processing Systems*, 2022.

Loshchilov, I. and Hutter, F. Decoupled weight decay regularization. In *International Conference on Learning Representations*, 2019.

Marczak, D., Magistri, S., Cygert, S., Twardowski, B., Bagdanov, A. D., and van de Weijer, J. No task left behind: Isotropic model merging with common and task-specific subspaces. In *International Conference on Machine Learning*, 2025.

Nasery, A., Hayase, J., Koh, P. W., and Oh, S. Pleas-merging models with permutations and least squares. In *Proceedings of the IEEE conference on Computer Vision and Pattern Recognition*, 2025.

Netzer, Y., Wang, T., Coates, A., Bissacco, A., Wu, B., and Ng, A. Y. Reading digits in natural images with unsupervised feature learning. In *Neural Information Processing Systems Workshops*, 2011.

Panariello, A., Marczak, D., Magistri, S., Porrello, A., Twardowski, B., Bagdanov, A. D., Calderara, S., and van de Weijer, J. Accurate and efficient low-rank model merging in core space. In *Advances in Neural Information Processing Systems*, 2025.

Radford, A., Kim, J. W., Hallacy, C., Ramesh, A., Goh, G., Agarwal, S., Sastry, G., Askell, A., Mishkin, P., Clark, J., Krueger, G., and Sutskever, I. Learning transferable visual models from natural language supervision. In *International Conference on Machine Learning*, 2021.

Raffel, C., Shazeer, N., Roberts, A., Lee, K., Narang, S., Matena, M., Zhou, Y., Li, W., and Liu, P. J. Exploring the limits of transfer learning with a unified text-to-text transformer. *Journal of Machine Learning Research*, 21, 2020.

Raghu, M., Gilmer, J., Yosinski, J., and Sohl-Dickstein, J. Svcca: Singular vector canonical correlation analysis for deep learning dynamics and interpretability. In *Advances in Neural Information Processing Systems*, 2017.

Rinaldi, F., Capitani, G., Bonicelli, L., Crisostomi, D., Bolelli, F., Ficarra, E., Rodolà, E., Calderara, S., and Porrello, A. Update your transformer to the latest release: Re-basin of task vectors. In *International Conference on Machine Learning*, 2025.

Rinaldi, F., Panariello, A., Salici, G., Liu, F., Ciccone, M., Porrello, A., and Calderara, S. Gradient-sign masking for task vector transport across pre-trained models. In *International Conference on Learning Representations*, 2026.

Singh, S. P. and Jaggi, M. Model fusion via optimal transport. In *Advances in Neural Information Processing Systems*, 2020.

Stallkamp, J., Schlipsing, M., Salmen, J., and Igel, C. The german traffic sign recognition benchmark: a multi-class classification competition. In *IJCNN*, 2011.

Stoica, G., Bolya, D., Bjorner, J. B., Ramesh, P., Hearn, T., and Hoffman, J. Zipit! merging models from different tasks without training. In *International Conference on Learning Representations*, 2024.

Turc, I., Chang, M.-W., Lee, K., and Toutanova, K. Well-read students learn better: On the importance of pre-training compact models. *arXiv preprint arXiv:1908.08962*, 2019.

Wang, A., Singh, A., Michael, J., Hill, F., Levy, O., and Bowman, S. R. GLUE: A multi-task benchmark and analysis platform for natural language understanding. In *International Conference on Learning Representations*, 2018.

Williams, A., Nangia, N., and Bowman, S. A broad-coverage challenge corpus for sentence understanding through inference. In *Proceedings of the 2018 Conference of the North American Chapter of the Association for Computational Linguistics: Human Language Technologies, Volume 1 (Long Papers)*, 2018.

Williams, A. H., Kunz, E., Kornblith, S., and Linderman, S. Generalized shape metrics on neural representations. In *Advances in Neural Information Processing Systems*, 2021.

Wortsman, M., Ilharco, G., Gadre, S. Y., Roelofs, R., Gontijo-Lopes, R., Morcos, A. S., Namkoong, H., Farhadi, A., Carmon, Y., Kornblith, S., et al. Model soups: averaging weights of multiple fine-tuned models improves accuracy without increasing inference time. In *International Conference on Machine Learning*, 2022a.

Wortsman, M., Ilharco, G., Kim, J. W., Li, M., Kornblith, S., Roelofs, R., Lopes, R. G., Hajishirzi, H., Farhadi, A., Namkoong, H., and Schmidt, L. Robust fine-tuning of zero-shot models. In *Proceedings of the IEEE conference on Computer Vision and Pattern Recognition*, 2022b.

Xiao, J., Ehinger, K. A., Hays, J., Torralba, A., and Oliva, A. Sun database: Exploring a large collection of scene categories. *International Journal of Computer Vision*, 2016.

Yadav, P., Tam, D., Choshen, L., Raffel, C., and Bansal, M. TIES-merging: Resolving interference when merging models. In *Advances in Neural Information Processing Systems*, 2023.

## A. Closed-form Derivation of the Transport Rule

In this Appendix, we derive the closed-form solution for the transported update  $\tau_B$  starting from the surrogate objective introduced in the main text. Recall the surrogate problem obtained after Procrustes alignment:

$$\min_{\tau_B} \|H_{\text{in},A}(\tau_A^\top - T_{\text{in}}\tau_B^\top T_{\text{out}}^\top)H_{\text{out},A}^\top\|_F^2. \quad (12)$$

Define the error matrix

$$E := \tau_A^\top - T_{\text{in}}\tau_B^\top T_{\text{out}}^\top. \quad (13)$$

Then Eq. (12) can be written compactly as

$$\min_{\tau_B} \|H_{\text{in},A}EH_{\text{out},A}^\top\|_F^2. \quad (14)$$

Under the injectivity conditions discussed in Sec. B, the linear map  $E \mapsto H_{\text{in},A}EH_{\text{out},A}^\top$  has a trivial null space on the aligned subspace. Consequently, the minimum of Eq. (14) is attained if and only if

$$E = 0. \quad (15)$$

Substituting Eq. (13) and solving for  $\tau_B$  yields

$$T_{\text{in}}\tau_B^\top T_{\text{out}}^\top = \tau_A^\top. \quad (16)$$

Multiplying by  $T_{\text{in}}^\top$  on the left and  $T_{\text{out}}$  on the right, and using the row-orthonormality of the Procrustes maps, we obtain

$$\tau_B^\top = T_{\text{in}}^\top \tau_A^\top T_{\text{out}}, \quad (17)$$

which gives the transport rule

$$\tau_B = T_{\text{out}}\tau_A T_{\text{in}}^\top. \quad (18)$$

## B. Injectivity and Rank Conditions

We justify the injectivity assumption used in the main text and in Sec. A.

**Lemma B.1.** *Let  $H_{\text{in},A} \in \mathbb{R}^{M \times d_{\text{in},A}}$  and  $H_{\text{out},A} \in \mathbb{R}^{M \times d_{\text{out},A}}$  have full column rank. Then the linear map*

$$\Phi : E \mapsto H_{\text{in},A}EH_{\text{out},A}^\top \quad (19)$$

*is injective.*

*Proof.* Using the vectorization operator and the Kronecker product, we have

$$\text{vec}(H_{\text{in},A}EH_{\text{out},A}^\top) = (H_{\text{out},A} \otimes H_{\text{in},A}) \text{vec}(E). \quad (20)$$

Since both  $H_{\text{in},A}$  and  $H_{\text{out},A}$  have full column rank, the Kronecker product  $H_{\text{out},A} \otimes H_{\text{in},A}$  has full column rank as well. Therefore,  $\text{vec}(H_{\text{in},A}EH_{\text{out},A}^\top) = 0$  implies  $\text{vec}(E) = 0$ , and hence  $E = 0$ .  $\square$

In practice, exact full-rank conditions are not required. Procrustes alignment isolates the dominant shared subspaces of the two representation spaces and preserves their geometry, ensuring that the map  $\Phi$  is injective on the aligned subspace spanned by the observed activations.

## C. Relation to Pseudo-Inverse Solutions

A natural approach to solving the original transport objective Eq. (4) is to derive a normal-equation solution by explicitly solving a least-squares problem. Formally, this yields

$$\tau_B^\top = (H_{\text{in},B}^\top H_{\text{in},B})^\dagger H_{\text{in},B}^\top G_A H_{\text{out},B} (H_{\text{out},B}^\top H_{\text{out},B})^\dagger, \quad (21)$$

where  $(\cdot)^\dagger$  denotes the Moore–Penrose pseudo-inverse.

However, this formulation is often numerically unstable in practice. When the two models differ in width, the activation Gram matrices  $H_{\text{in},B}^\top H_{\text{in},B}$  and  $H_{\text{out},B}^\top H_{\text{out},B}$  are frequently ill-conditioned or rank-deficient, especially when estimated from a finite number of samples.

Our Procrustes-based conditioning step can be interpreted as an orthogonal change of basis that aligns the dominant shared subspaces of the two representation spaces. In the aligned coordinates, the Gram matrices become well-conditioned, and the pseudo-inverse solution reduces to the closed-form transport rule derived in Sec. A.

## D. Experimental setting

**Models.** In the vision experiments, we employ CLIP models (Radford et al., 2021) with architectures and weights obtained from Open-CLIP (Cherti et al., 2023). We consider three distinct architectural configurations: (i) **Width scaling**: transferring from a standard ViT-B/16 pre-trained on LAION-2B to a wider ViT-B+ variant pre-trained on LAION-400M; (ii) **Same architecture**: transferring between identical ViT-B/16 models pre-trained on different distributions, specifically DataComp-XL and LAION-2B; (iii) **Width and depth scaling**: transferring across both depth and width from a ViT-B/16 to a ViT-L/14, both pre-trained on DataComp-XL. Unless otherwise specified, model  $A$  denotes the smaller or source model and model  $B$  the larger or target model. For the language experiments, we utilize T5 encoder-decoder models (Raffel et al., 2020) of varying scales, specifically transferring from T5-3B to T5-Large.

**Task Updates.** The task-specific updates  $\tau_A$  are derived by fine-tuning the base model  $A$  on the target downstream task via standard supervised objectives. Following the optimization protocol established by Ilharco et al. (2023), we fine-tune for 2000 iterations with a batch size of 128. We

employ the AdamW optimizer (Loshchilov & Hutter, 2019) with a peak learning rate of  $1 \times 10^{-5}$ , a weight decay of 0.1, and a cosine annealing schedule preceded by 200 warm-up steps. In accordance with Cherti et al. (2023), the text encoder backbone remains frozen throughout the training process. We then transport  $\tau_A$  to model  $B$  using the proposed method, without performing any additional optimization or gradient-based updates on model  $B$ .

**Few-shot protocol.** We evaluate our method using a  $B$ -shot protocol, where  $B \in \{1, 2, 5, 10, 20\}$  denotes the number of batches sampled, each with a fixed batch size of 32, to characterize the representation spaces of models  $A$  and  $B$ . For each value of  $B$ , we draw training batches uniformly at random to construct the support set required for Procrustes alignment Eq. (5). Additionally, to maintain consistency with existing literature, we also report results under a standard  $K$ -shot evaluation protocol with  $K \in \{1, 2, 5, 10, 20\}$  examples per class.

**Evaluation.** For vision tasks, we evaluate classification accuracy on standard benchmarks following the CLIP evaluation protocol. For language tasks, we report accuracy on each dataset. All results are averaged across tasks unless otherwise specified.

## E. Additional Experiments

### E.1. Sequence Length Alignment Strategies.

To resolve sequence length mismatches between the source  $\theta_A$  and target  $\theta_B$ , we evaluate three distinct alignment strategies. These are necessitated by the fact that different ViT configurations may encode images into varying numbers of patches, resulting in disparate token sequence lengths  $L^A$  and  $L^B$ .

The *mean* strategy serves as a baseline by averaging the feature representations across the sequence dimension, effectively removing spatial granularity. The *interpolation* strategy treats the token sequences as 1D signals, employing a linear interpolation to resample the source sequence to the target’s length. Finally, *interpolation2d* leverages the spatial inductive bias of the Vision Transformer by reshaping the 1D token sequence into a 2D grid that mirrors the original image’s patch layout. A bilinear interpolation is then applied to this grid to match the target resolution before flattening the result back into a sequence.

As shown in Tab. 5, the *interpolation2d* strategy consistently yields the highest accuracy across all batch sizes, significantly outperforming both the 1D linear and mean-based approaches. This emphasizes the importance of preserving the spatial topology of the features: by maintaining the geometric correspondence between patches, the method more effectively transfers the task-specific knowledge distilled

by the source model. Notably, these sequence-level adjustments are exclusive to the vision domain. In contrast, for the T5 experiments (Tabs. 2 and 9), no sequence interpolation is necessary. Because T5 natively supports variable-length text sequences, input lengths can be adjusted prior to activation computation to directly match source and target representations, allowing the transport process to be performed without additional preprocessing.

### E.2. Extended Results on Width Scaling.

We provide a comprehensive evaluation of the  $(A \rightarrow B)$  transport direction under varying  $K$ -shot settings in Tab. 6, illustrating how performance scales as the number of labeled samples per class increases. Complementary results for the reverse transport direction ( $B \rightarrow A$ ) are detailed in Tabs. 7 and 8, utilizing both batch-based  $B$ -shot and class-balanced  $K$ -shot protocols. Collectively, these findings confirm that THESEUS is robust across diverse sampling strategies and consistently yields improvements, even when the target model already exhibits a strong zero-shot baseline.

### E.3. Language.

Following the experiment setting of Rinaldi et al. (2025), we consider the model  $\theta = \{\phi, \omega\}$  composed of a pre-trained feature extractor  $\phi$  and a classification head  $\omega$ . We transport the task vector  $\tau_A^\phi$  from model  $A$  (T5-3b) to the target feature extractor  $\phi_B$  (T5-Large). We then refrain from training a new classifier for the target model and instead reuse source fine-tuned head  $\omega_{ft}^A$ . This allows us to evaluate whether the transported representation space aligns with the source model’s classification logic without additional head optimization. As baselines, we report the performance of the target backbone  $\theta_B$  equipped with a randomly initialized classification head, alongside a fully fine-tuned version of  $\theta_B$  where both the encoder and head are optimized for the target task. As can be seen in Tab. 9, the accuracy gain is proportional yet consistent across different numbers of batches  $B$  for the alignment, in all the cases the baseline  $\theta_B$  is outperformed.

## F. Dataset Details

### F.1. Visual Datasets.

We evaluate our method on a diverse suite of vision classification benchmarks, covering a wide range of domains from natural images to satellite imagery:

- **EuroSAT:** A remote sensing dataset based on Sentinel-2 satellite imagery, comprising 27 000 geo-referenced samples across 10 distinct classes (Helber et al., 2019).
- **SVHN:** A digit recognition benchmark containing 73 257 real-world images of house numbers across

Table 5. Ablation on Interpolation Modes. Performance across datasets for different batch sizes  $B$  and interpolation strategies. Results are reported as accuracy (%).

Model	$B$	Interpolation	EUROSAT	SVHN	GTSRB	RESISC45	DTD	CARS	MNIST	SUN397	AVG ( $\Delta$ Acc)
$\theta_B$ zero-shot	–	–	56.69	62.66	55.46	68.51	58.19	88.81	76.47	72.42	67.40 (+0.00)
$\theta_B$ fine-tune	–	–	98.66	97.70	98.77	95.40	83.29	92.43	99.64	79.91	93.23 (+25.83)
THESEUS	1	mean	59.60	63.21	55.47	68.45	58.33	88.89	79.00	72.53	68.19 (+0.79)
		interpolate	57.96	62.91	56.88	68.75	58.85	88.92	79.33	72.49	68.23 (+0.83)
		interpolate2d	66.31	76.55	63.57	70.33	60.00	88.86	88.14	72.67	<b>73.30 (+5.90)</b>
THESEUS	2	mean	58.31	62.96	56.72	68.73	58.39	88.83	79.10	72.47	68.44 (+1.04)
		interpolate	62.94	63.33	57.13	69.03	58.97	88.98	78.66	72.64	68.96 (+1.56)
		interpolate2d	70.00	73.86	68.38	72.59	59.95	88.85	88.64	72.75	<b>74.38 (+6.98)</b>
THESEUS	5	mean	62.33	63.20	58.16	68.89	59.41	88.88	80.94	72.88	69.34 (+1.94)
		interpolate	62.31	64.25	58.79	69.71	59.81	89.08	82.27	72.77	69.88 (+2.48)
		interpolate2d	71.14	79.66	69.78	72.27	62.02	88.95	93.88	73.01	<b>76.34 (+8.94)</b>

Table 6. Width Scaling (Small  $\rightarrow$  Big) Cross-dataset performance ( $A$ : laion2b  $\rightarrow$   $B$ : laion400m). Results are reported for varying support set sizes  $K$

Model	$K$	EUROSAT	SVHN	GTSRB	RESISC45	DTD	CARS	MNIST	SUN397	AVG ( $\Delta$ Acc)
$\theta_B$ zero-shot	–	50.92	39.23	49.63	64.53	55.48	84.53	57.06	68.67	58.76 (+0.00)
$\theta_B$ fine-tune	–	98.96	91.08	98.63	92.59	77.81	87.65	99.63	76.76	90.39 (+31.63)
$\theta_A$ fine-tune	–	98.69	97.45	98.64	95.65	82.24	91.53	99.61	79.86	92.96 (+34.20)
THESEUS	1	60.79	55.73	57.39	67.48	57.34	85.02	61.67	70.76	<b>64.52 (+5.76)</b>
THESEUS	2	61.46	56.07	59.03	68.01	58.56	85.06	68.19	70.81	<b>65.90 (+7.14)</b>
THESEUS	5	64.58	55.20	59.05	69.18	59.25	85.17	77.57	70.93	<b>67.62 (+8.86)</b>
THESEUS	10	65.51	56.86	59.72	69.48	60.48	85.16	76.26	71.28	<b>68.09 (+9.33)</b>
THESEUS	20	66.83	60.33	58.25	70.03	60.53	85.51	78.38	72.12	<b>69.00 (+10.24)</b>

10 classes extracted from Google Street View (Netzer et al., 2011).

- **GTSRB:** The German Traffic Sign Recognition Benchmark, a standard for autonomous driving tasks featuring 51 839 images across 43 traffic sign categories (Stallkamp et al., 2011).
- **RESISC45:** A high-resolution remote sensing dataset containing 31 500 images from Google Earth, categorized into 45 scene classes to evaluate fine-grained aerial classification (Cheng et al., 2017).
- **DTD:** The Describable Textures Dataset, consisting of 5640 texture-centric images organized into 47 perceptual categories (Cimpoi et al., 2014).
- **Stanford Cars:** A fine-grained classification dataset comprising 16 185 images across 196 categories of cars, distinguished by make, model, and year (Krause et al., 2013).
- **MNIST:** The Modified National Institute of Standards and Technology database, a foundational benchmark for handwritten digit recognition containing 70 000 grayscale images across 10 classes (Lecun et al., 1998).

- **SUN397:** A large-scale scene understanding benchmark consisting of 108 754 images covering 397 categories, ranging from indoor environments to diverse outdoor landscapes (Xiao et al., 2016).

## F.2. Textual Datasets

- **SNLI:** Stanford Natural Language Inference dataset, containing 570 000 sentence pairs labeled for entailment, contradiction, or neutral (Group et al., 2022).
- **MNLI:** The Multi-Genre Natural Language Inference dataset contains 433 000 sentence pairs annotated with textual entailment information across various genres (Williams et al., 2018).
- **RTE:** Recognizing Textual Entailment dataset, with 2490 examples for training, 277 for validation, and 3000 for testing, divided into two classes (Wang et al., 2018).
- **QNLI:** Question Natural Language Inference dataset, contains 104 743 training examples into two classes (Wang et al., 2018).
- **SCITAIL:** A science entailment dataset built from science question answering, with 23 596 training examples of two classes (Khot et al., 2018).

Table 7. **Width Scaling (Big → Small)** Cross-dataset performance ( $A$ : laion400m →  $B$ : datacomp\_xl). Results are reported for varying support set sizes  $\mathcal{K}$

Model	$\mathcal{K}$	EUROSAT	SVHN	GTSRB	RESISC45	DTD	CARS	MNIST	SUN397	AVG ( $\Delta$ Acc)
$\theta_B$ zero-shot		56.69	62.66	55.46	68.51	58.19	88.81	76.47	72.42	67.40 (+0.00)
$\theta_B$ fine-tune		98.66	97.70	98.77	95.40	83.29	92.43	99.64	79.91	93.23 (+25.83)
THESEUS	1	62.95	73.56	66.99	71.03	60.16	88.79	83.31	73.18	<b>72.50</b> (+5.10)
	2	68.01	74.19	67.19	70.89	60.53	88.91	88.15	73.26	<b>73.89</b> (+6.49)
	5	68.35	75.92	71.20	72.68	62.13	88.92	92.25	73.22	<b>75.58</b> (+8.18)
	10	73.16	76.93	67.63	73.44	62.93	88.89	91.98	73.21	<b>76.02</b> (+8.62)
	20	70.84	82.82	70.63	73.89	63.62	89.03	94.33	73.38	<b>77.32</b> (+9.92)

Table 8. **Width Scaling (Big → Small)** Cross-dataset performance ( $A$ : laion400m →  $B$ : datacomp\_xl). Results for varying number of alignment batches  $B$ .

Model	$B$	EUROSAT	SVHN	GTSRB	RESISC45	DTD	CARS	MNIST	SUN397	AVG ( $\Delta$ Acc)
$\theta_B$ zero-shot		56.69	62.66	55.46	68.51	58.19	88.81	76.47	72.42	67.40 (+0.00)
$\theta_B$ fine-tune		98.66	97.70	98.77	95.40	83.29	92.43	99.64	79.91	93.23 (+25.83)
THESEUS	1	66.31	76.55	63.57	70.33	60.00	88.86	88.14	72.67	<b>73.30</b> (+5.90)
THESEUS	2	70.00	73.86	68.38	72.59	59.95	88.85	88.64	72.75	<b>74.38</b> (+6.98)
THESEUS	5	71.14	79.66	69.78	72.27	62.02	88.95	93.88	73.01	<b>76.34</b> (+8.94)
THESEUS	10	71.75	79.73	69.58	72.33	62.25	89.00	94.12	73.16	<b>76.49</b> (+9.09)
THESEUS	20	72.36	80.33	68.58	74.01	62.61	88.97	94.30	73.24	<b>76.80</b> (+9.40)

Table 9. **Width Scaling (Big → Small)** Cross-dataset performance ( $A$ : T5-3B →  $B$ : T5-Large). Transfer of task-specific feature extractors. Results for varying number of alignment batches  $B$ .

Model	$B$	MNLI	QNLI	RTE	SCITAIL	SNLI	AVG ( $\Delta$ Acc)
$\theta_B$	—	32.23	48.05	48.38	50.77	32.44	42.37 (+0.00)
$\theta_B$ fine-tune	—	89.80	94.27	83.59	95.86	91.83	91.09 (+48.72)
THESEUS	20	57.01	50.56	49.46	50.77	57.24	<b>53.01</b> (+10.64)
THESEUS	50	54.52	56.31	50.12	53.45	60.42	<b>54.96</b> (+12.59)
THESEUS	100	55.66	59.49	50.98	63.11	64.89	<b>58.83</b> (+16.46)